

3-Tesla Active-Shield MR Images : Current Status of Recent Development

최보영

Department of Biomedical Engineering, Kangnam St. Mary's Hospital,

College of Medicine, The Catholic University of Korea

INTRODUCTION

The first magnetic resonance imaging experiments were conducted with nuclear magnetic resonance (NMR) line scanning (1) and projection reconstruction (2) methods. While these methods established the feasibility of the magnetic resonance imaging (MRI) approach, they were characterized with relatively low spatial resolution (1,2). Nonetheless, technological advances in gradient design (3) and spatial encoding methods (4,5) soon permitted an increase in achievable spatial resolution, thereby greatly improving the radiologic utility of MRI methods.

The need for enhanced spatial resolution in magnetic resonance arises from the desire to more precisely visualize small structures both on conventional and angiographic images. Increased spatial resolution also results in reduced susceptibility artifacts in echo-based MR imaging in part due to the associated increases in receiver bandwidths (6,7). In addition, enhanced spatial resolution leads to superior image interpolation required in generating MR angiograms (MRA).

Unfortunately, since magnetic resonance is an inherent technique, image resolution cannot be continuously increased without significantly compromising image quality and signal-to-noise ratio (8-11). As these two characteristics progressively deteriorate, the ability to detect the structure of interest, or the visibility, also degrades. Visibility (V) can be defined as the product of the contrast-to-noise ratio (CNR) and the square root of the number of pixels (p) occupied by the object of interest. It is expressed as follows: $V = \text{CNR} \sqrt{p}$. The importance of determining appropriate spatial resolution based on visibility rather than signal-to-noise criteria alone has been addressed (12).

At 1.5T, increases in spatial resolution have often been associated with the use of specialized local surface (13) or phased array (14) radio frequency (RF) coils in order to maximize the available signal-to-noise at this field strength. In addition, signal processing methods may help enhance signal-to-noise while preserving, as much as possible, edge definition (15-16). Using a combination of these approaches, excellent high resolution images have been obtained from the human skin (17), the extremities and cartilage (18-20), the trabecular bone (21-22), the inner ear (23-27), the eye (28-31), and the facial nerves

(32-34). Increased spatial resolution has also proven valuable in MRA studies where higher resolution 3D data sets provide vessel visualization (35-36). Indeed, increased spatial resolution leads not only to the visualization of more vessels but also in the ability to differentiate progressively smaller structures. It is known for instance that vessel visibility is determined by the position of the structure of interest within the voxel grid (37). Vessels contained entirely within one voxel are thus brighter than when positioned between voxels. This is a partial volume effect that can be reduced with increased matrix size. Nonetheless, as resolution continues to increase, signal to noise to degrade to such an extent that visibility becomes compromised and the number of vessels observed no longer continues to increase. Similarly, while high resolution approaches increase functional localization in functional MRI by reducing partial volume effects, this is associated both with a significant increase in scan times and a reduction in signal to noise (38).

Despite limitations in signal to noise even with high field systems operating at 1.5T excellent high resolution studies of the human brain have been conducted at this field strength. Using phased array detectors and an automated intensity correction algorithm, for instance, Wa et al. (39) have been able to obtain good spoiled gradient recalled volume acquisition images. In these studies, an in-plane pixel size of 0.47-0.66mm was obtained using a 0.7 mm slice thickness. Alternatively, using a fast spin echo approach were able to obtain 512×512 image with an in-plane resolution of 0.27-0.33 mm with a 1.5-3 mm slice thickness and an acquisition time of only 8.5 minutes. Similarly, Feinberg et al. (40) using the gradient-SE (GRASE) technique and partial k-space sampling, were able to obtain 2D-1024 matrix images of the human head in only 4 minutes, 20 seconds. The resulting images contained a 0.28×0.27 mm in-plan resolution from a 4 mm slice and displayed many small anatomic structures including the cochlea of the inner ear, vascular details, and the cranial nerves.

Given available field strength and total acquisition time, the aforementioned studies illustrate the potential of high resolution MRI. This conclusion can be further amplified by work performed at 4T (41-42) where high resolution modified driven equilibrium Fourier transform (MDEFT) images were obtained using a 512×512 matrix. These images had a 400-500 μm in-plane resolution from a 5 mm slice and revealed exquisite anatomical detail and gray/white matter contrast. Moreover, they display remarkable signal to noise in very high field (VHF) MRI, despite the use of standard volumetric head coils (43).

Recently, a series of 1K×1K gradient echo images with a 200 μm in-plane resolution (44-45) have been obtained from the human head at 8 Tesla (46-47) using standard transvers electromagnetic (TEM) volumetric coils (48). These images display good in-plane resolution and enhancement of the venous vasculature. In addition, they highlight the tremendous magnetic susceptibility obtained at ultra high field strengths.

MATERIALS AND METHODS

High resolution gradient recalled echo images were acquired at 128 MHz using a 3 instrument. It consists of a 3 Tesla/64 cm superconducting magnet manufactured by Oxford Magnet Technology LTD. (Witney, England) and customized gradient coil by Tesla Engineering Limited (Sussex, England). This magnet is independently ordered for the active shielded type with the weight of 11 tons. And, it is positioned within a magnetic shield constructed from annealed low carbon steel (grade 1006). Using a combination of superconductive shims located within the cryostat and resistive shims located in a specialized shim insert, the 3T magnet achieved a homogeneity of 3.78 ppm over a 40 cm diameter spherical volume established on a 12-plane plot. The gradient system utilized in these studies consists of an asymmetric torque free gradient insert for whole body imaging. The gradient amplifier is capable of delivering 650V/430A on each gradient axis, and provided by MTS (MTS Systems Corporation, Horsham PA, USA). And, spectrometer has a four channel system.

All images in this study were acquired with a Magnus 2.1 for Magnum 3T (Medinus LTD Korea). It is equipped with Magnus Software and is able to support basic acquisition pulse sequences for fast EPI imaging, broad line imaging, 3D imaging, angiography and spectroscopy. The RF front end of the 3T system is comprised of a high power TR switch. Nonmagnetic narrow band Ga/As field effect transistor (FET) preamplifiers (Advanced Receiver Research Burlington, CT, U.S.A) complete the front end allowing close proximity of the RF front end to the NMR coil. The quality of the receiver chain with the Magnum console was measured by examining the noise performance.

Spin echo (SE) pulse sequence was employed for T1-weighted MR images. However, for proton density and T2-weighted MR images, we used fast spin echo (FSE) with the echo train length of 8 or 16.

Radio frequency power at 128 MHz was provided by RF amplifiers constructed specifically for this project by AMT (Herley Company, Anaheim, CA, USA). Images were acquired with birdcage volumetric head coil and TEM head coil. The TEM coil was designed to operate quadrature and was constructed from a group of 16 TEM struts enclosed in a copper shield.

RESULTS

T1-weighted axial SE images obtained from a brain of normal volunteer at 3T using 500ms, TE 10 ms and 256×256 matrix are displayed in Fig. 1. These images were obtained with a 4 mm slice thickness, a 20 cm FOV, using conventional SE pulse sequence. As can be seen, the contrast between white and gray matter is remarkable. And, structures of basal ganglia, internal and external capsules as well as ventricles are well discriminated.

Figure 2 shows T2-weighted axial FSE images with high resolution of 512x512 matrix, TR 4000 ms, TE 108 ms. Note the substantial degree of vascular structure in detail. It is clearly differentiable for putamen and globus pallidus in basal ganglia. T2-weighted coronal and sagittal images are shown in Figs 3 and 4. Fine structural components in cerebellum are marked. Proton density axial images were shown in Fig. 5. For acquisition of proton density image, we used FSE by 4 excitation pulse with TR 2000 ms, TE 16 ms, NEX 2. White matter has rather dark signal than gray matter. Figure 6 shows fast spin echo FLAIR images with ETL 8, TI 140 ms, TR 6000 ms and TE 16 ms. CSF has completely dark signal than any other tissue. Most of fat signal was suppressed in fast spin echo STIR image in Fig. 7 with TI 2200 ms, TR 9000 ms and TE 96 ms. Note the fat tissue near skull has dark signal. MR angiography is presented by 3D-time of flight (TOF) technique with TR 30 ms, TE 6.6 ms, FA 25, NEX 1 in Fig. 8. Peripheral vessels as well as major vessels are clearly demonstrated without problematic artifacts.

T1 and T2-weighted coronal and sagittal MR images of knee are shown in Fig. 9 and 10 respectively. Lateral and medial meniscus are well denoted. For acquisition of T1-weighted coronal image, we used TR 500 ms, TE 17.4 ms, slice thickness 4 mm and NEX 1. And, T2-weighted sagittal images, we used FSE with ETL 16, TR 5500 ms, TE 88 ms, slice thickness 4 mm and NEX 1. Anterior cruciate ligament is well delineated as a dark sign intensity.

Figures 11 and 12 show T1- and T2-weighted MR image of foot with identical parameters for knee scans. The individual bones and joints are clearly seen.

T1, T2 and T2*-weighted MR images of wrist were obtained in Fig. 13. In particular, we used gradient echo of spoiled pulse in steady state (GESPSS) with TR 450 ms, TE 15 ms, NEX 2 and flip angle 22°. The ligaments and muscle as well as entire carpal and metacarpal bones and joints are well visualized.

DISCUSSION

Given the excellent technological performance of modern MRI scanners, the ability to acquire high resolution images with this modality is governed almost exclusively by available signal to noise. Thus, while excellent images can be acquired at 1.5T, this field strength lacks the inherent signal to noise to make high resolution imaging feasible. As such, note that when conventional acquisition methods are utilized at 1.5T, it is difficult to obtain a resolution with pixel volume much below 1 mm³. Indeed, using a standard SE pulse sequence and a bird-cage quadrature head coil configuration with a state-of-the-art clinical scanner, images obtained with a 1 mm³ pixel volume yielded little or no useful diagnostic information. In contrast at 3T MRI system, high resolution images (pixel volume ≤ 0.1 mm³) can be obtained using standard imaging sequences and RF head coils without difficulty. This is the case despite the use

larger receiver bandwidths and less than fully relaxed spin excitation conditions.

T2-weighted MR image displayed in Fig. 2 was presented for appropriate reasons in that represent the trial attempt to obtain high resolution results at 3T. In addition to provide high contrast of compatible quality in MR image, it does reveal the potential of high field magnet resonance imaging for increasing spatial resolution. While SNR of 3T system is increased approximately 2.7 times compared with prevalent 1.5T system, the contrast in 3T system was not proportionally increased like SNR. However, as SNR increases, the total scan time could be significantly reduced.

In addition to T1-weighted MR image (Fig. 1), T2-weighted MR images were displayed in Figs. 2-4. Note the vascular detail in these images, despite the use of a standard FSE pulse sequence. Much of this vascular anatomy is venous in origin. Nonetheless, there are literally hundreds of minute vessels visible in these images. This speaks to the tremendous potential of a high field MRI system in obtaining high-resolution MRA results (Fig. 8). At the same time while the pixel resolution on these images is outstanding, it cannot be directly related to true in-plane resolution due to inherent physiological motion. Thus, it may become important to gate image acquisition to cardiac or other physiological motion in order to help ensure that pixel resolution can be directly correlated to true resolution.

Nonetheless, the ability to obtain high resolution MR images will remain ultimately dictated by the Boltzmann equation. This equation determines the distribution of the spin population in the up state relative to the down state as a result of temperature and field strength. Thus, given adequate spectrometer hardware, the only way to significantly enhance signal to noise is through a substantial increase in field strength.

The fundamental promise of a high field MRI system relies on increased image resolution and decreased scanning times, both of which are critically related to intrinsic signal to noise (49). It reflects signal to noise in the absence of T1, T2*, motion, flow, and scanner hardware effects. Intrinsic signal to noise, in turn, must increase with field strength. It is clear from the images contained herein that the intrinsic signal to noise ratio at 3T will be phenomenally possibly approaching a factor of 2.7 increase over a conventional 1.5T scanner. Given such performance, it is difficult to fully visualize the potential impact of high field MR imaging. Nonetheless, we had better insist on the present trends in signal to noise and high resolution imaging continue. Finally, it appears that the radiological sciences are destined to become increasingly field-strength oriented in nature.

Acknowledgment: Author would like to appreciate to all participants of CMC-Medinus 3T MRI project for their valuable assistance.

REFERENCE

1. Damadian R, Goldsmith M, Minkoff L. NMR scanning. In: NMR basic Principles and Progress. vol. 19 Diehl P, Fluck E, Kosfeld R, eds. Berlin: Springer-Verlag, 1981:1-16.
2. Lauterbur PC. Image formation by induced local interactions: example employing nuclear magnetic resonance. *Nature* 1973;242:190-191.
3. Mansfield P, Chapman B. Active magnetic screening of gradient coils in NMR imaging. *J Magn Reson* 1986;66:573-576.
4. Kumar A, Welti D, Ernst RR. NMR Fourier Zeugmatography. *J Magn Reson* 1975;18: 69-83.
5. Edelstein WA, Hutchison JMS. Spin warp NMR imaging and application to human whole-body imaging. *Phys Biol Med* 1990;25:751-756.
6. Young IR, Cox IJ, Bryant D, Bydder GM. The benefits of increasing spatial resolution as a means of reducing susceptibility artifacts due to field inhomogeneities. *Magn Reson Imag* 1988;6:585-590.
7. Abduljalil AM, Robitaille P-ML. Macroscopic susceptibility in ultra high field MRI. *J Comput Assist Tomogr* 1999;23:832-841.
8. Venkatesan R, Haacke EM. Role of high resolution in magnetic resonance (MR) imaging: applications to MR angiography, intracranial T1-weighted imaging, and image interpolation *Int Imag sys Technol* 1997;8:529-543.
9. Edelstein WA, Glover GH, Hardy CJ, Redington RW. The intrinsic signal-to-noise in NMR imaging. *Magn Reson Med* 1986;3:604-618.
10. Parker DL, Gullberg GT. Signal to noise efficiency in magnetic resonance imaging. *Med Phys* 1990;17:250-257.
11. Hoult DI, Richards RE. The signal to noise of the nuclear magnetic resonance experiment. *J Magn Reson* 1976;24:71-85.
12. Constable Henkelman RM. Contrast, resolution, and detectability in MR imaging. *J Comput Assist Tomogr* 1991;15:297-303.
13. Ackerman JJH, Grove TH, Wong GG, Grdian DG, Radda GK. Mapping of metabolites in whole animals by ³¹P NMR using surface coils. *Nature* 1980;283:167-170.
14. Roemer PB, Edelstein WA, Hayes CE, Souza SP, Mueller OM. The NMR phased array. *Magn Reson Med* 1990;16:192-225.
15. Mc Veigh ER, Henkelman RM, Bronskill MJ. Noise and filtration in magnetic resonance imaging. *Med Phys* 1985;12:586-591.
16. Ying K, Clymer BD, Schmalbrock P. Adaptive filtering for high resolution magnetic resonance images. *J Magn Reson Imag* 1996;6:367-377.

17. Idy-Peretti I, Bittoun J, Alliot FA, Richard SB, Querleux BG, Cluzan RV. Lymphedematous skin and subcutis: in vivo high resolution magnetic resonance imaging evaluation. *J Invest Dermatol* 1998;110:782-787.
18. Potter HG, Asnin-Ernberg L, Weiland AJ, Hotchkiss RN, Peterson MGE, McCormack RR. The utility of high-resolution magnetic resonance imaging in the evaluation of the triangular fibrocartilage complex of the wrist. *J Bone Joint Surg* 1997;79A:1675-1684.
19. Drape JL, Peretti I, Goettmann S, Guerin-Surville H, Bittoun J. Standard and high resolution magnetic resonance imaging of glomus tumors of nose and fingertips. *J Am Ac Dermatol* 1996;35:550-555.
20. Waldschmidt JG, Rilling RJ, Kajdacsy-Balla AA, Boynton MD, Erickson SJ. In vitro and in vivo MR imaging of hyaline cartilage: zonal anatomy, imaging pitfalls, and pathologic conditions. *Radiograph* 1997; 17:1387-1402.18-20.
21. Majumdar S, Genant HK, Grampp SS, Newitt DC, Troung VHLin Jc, Mathur A. Correlation of trabecular bone structure with age, bone mineral density, and osteoporotic status: in vivo studies in the distal radius using high resolution magnetic resonance imaging. *J Bone Mineral Res* 1997; 12:1111-12118.
22. Ouyang X, Selby K, Lang P, et al High resolution magnetic resonance imaging of the calcaneus: age-related changes in trabecular structure and comparison with dual X-r absorptiometry measurements. *Calcif Tissue Int* 1997;60:139-147.
23. Schmalbrock PM, Pruski J, Sun L, Rao A, Monroe J. Phased array RF coils for high-resolution MRI of the inner ear brain stem. *J Comput Assist Tomogr* 1995;19:8-14.
24. Brogan M, Chakeres DW, Schmalbrock P. High-resolution 3DFT MR imaging of the endolymphatic duct and soft tissue of the otic capsule. *AJNR* 1991;12:1-11.
25. Arnold B, Jager L, Grevers G. Visualization of inner ear structures by three-dimensional high resolution magnetic resonance imaging. *Am J Otol* 1996;17:480-485.
26. Dahm MC, Mack MG, Tykocinski M, Vogl TJ. Submillimeter imaging and reconstruction of the inner ear. *Am J Otol* 1997;18:S54-S56
27. Casselman JW, Kuhweide R, Deimling M, Ampe W, Dehaeme I, Meeus L. Constructive interference in steady state-3D FT MR imaging of the inner ear and cerebellopontine angle. *AJNR* 1993;14:47-57.
28. Ettl A, Kramer J, Daxer A, Koornneef L. High-resolution magnetic resonance imaging of the normal extraocular musculature. *Eye* 1997;11:93-97.
29. Mashima Y, Oshitari K, Imamura Y, Momoshima S, Shiga H, Oguchi Y. Orbital high resolution magnetic resonance imaging with fast spin echo in the acute stage of Leber hereditary optic neuropathy. *J Neurol Neurosurg Psychiatry* 1998;64:124-127.
30. Herrick RC, Hayman LA, Taber KH, Diaz-Marchan PJ, Kuo MD. Artifacts and pitfalls in MR imaging of the orbit: a clinical review. *Radiograph* 1997;17:707-724.

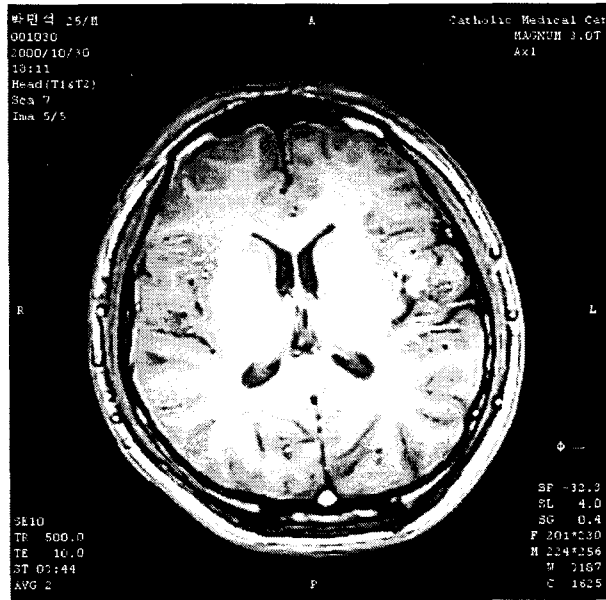
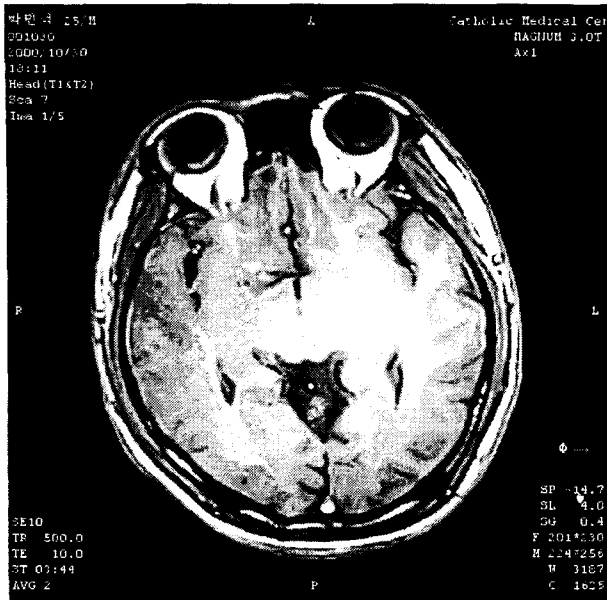


Figure 1. Typical T1-weighted axial MR images in normal volunteer using conventional spin echo pulse sequence. Parameters are TR 500ms, TE 10 ms, matrix 256×256, slice thickness 4mm, FOV 20 cm, NEX 1.

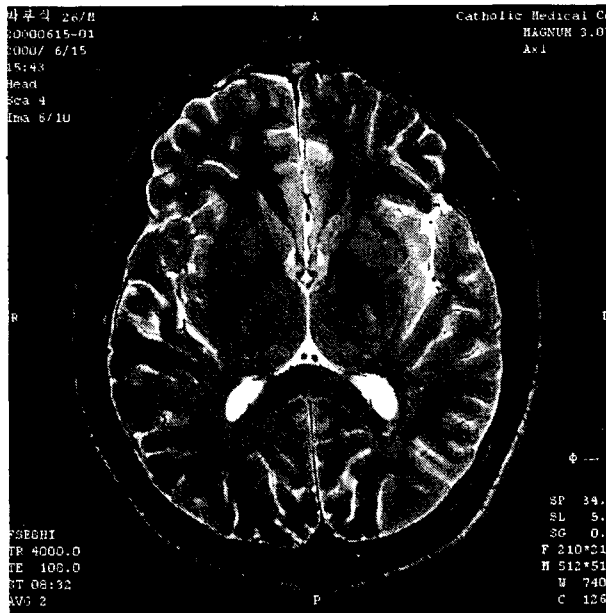
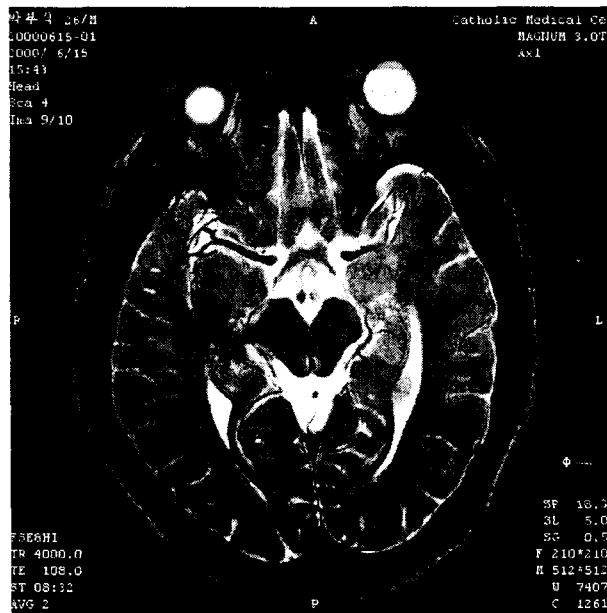


Figure 2. Typical T2-weighted axial MR images in normal volunteer using fast spin echo with ETL 8. Parameters are TR 4000ms, TE 108 ms, matrix 512×512, slice thickness 5mm, FOV 20 cm, NEX 2.

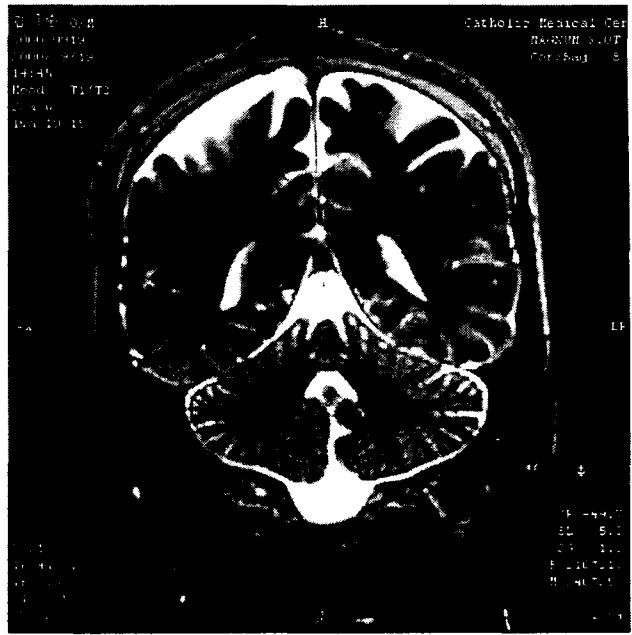
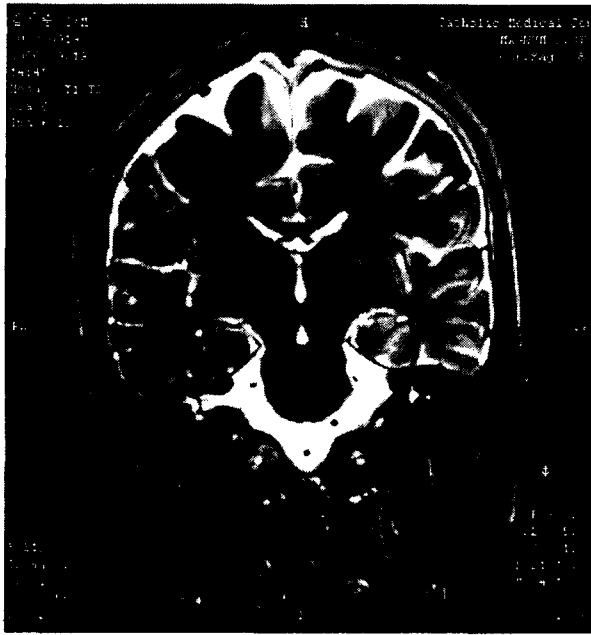


Figure 3. T2-weighted coronal MR images in normal volunteer using fast spin echo with ETL 12.

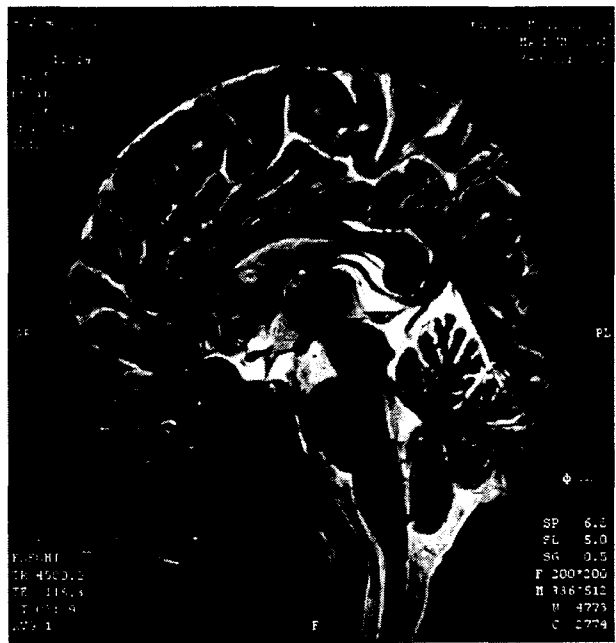
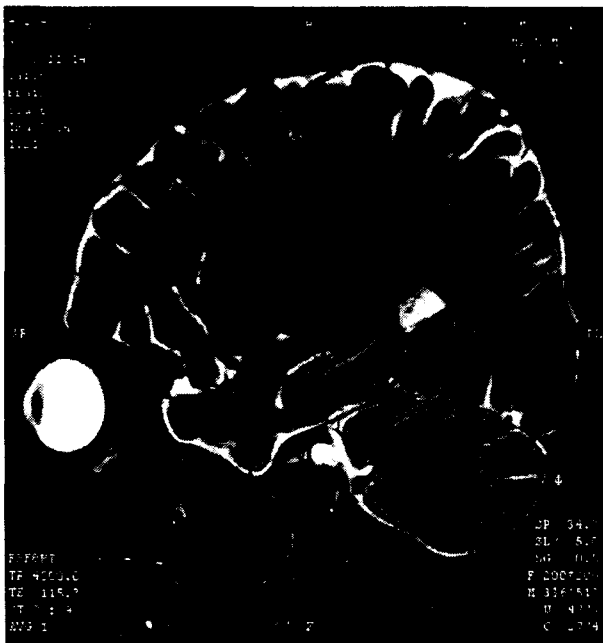


Figure 4. T2-weighted sagittal MR images in normal volunteer using fast spin echo with ETL 8.

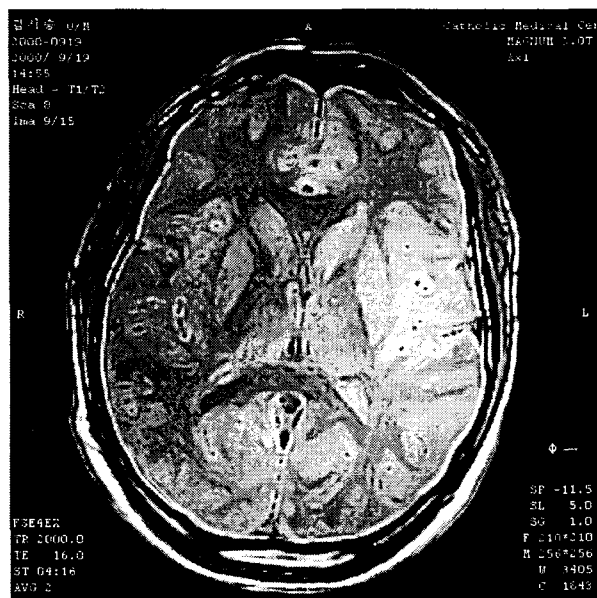
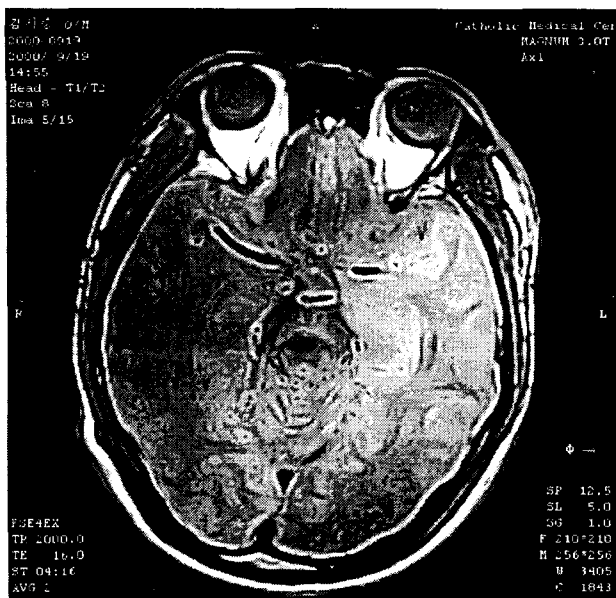


Figure 5. Proton density axial MR images using fast spin echo by 4 excitation pulse with TR 2000 ms, TE 16 ms, NEX 2.

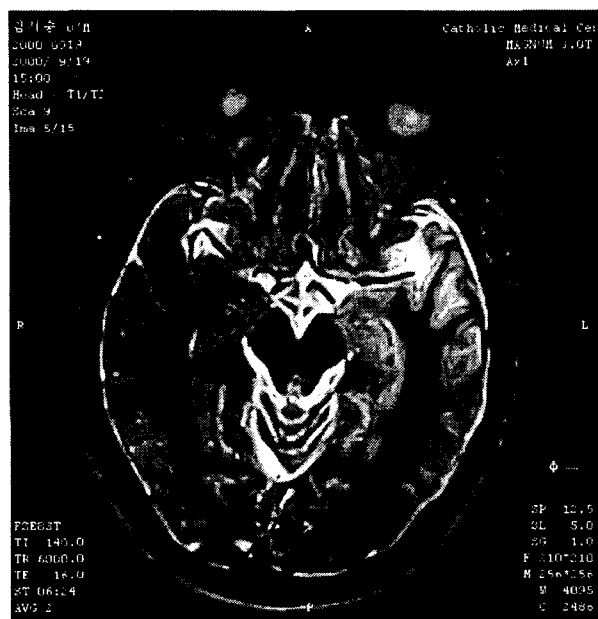


Figure 6. Fast Spin Echo FLAIR images with TI 140, TR 6000 and TE 16, NEX 2.

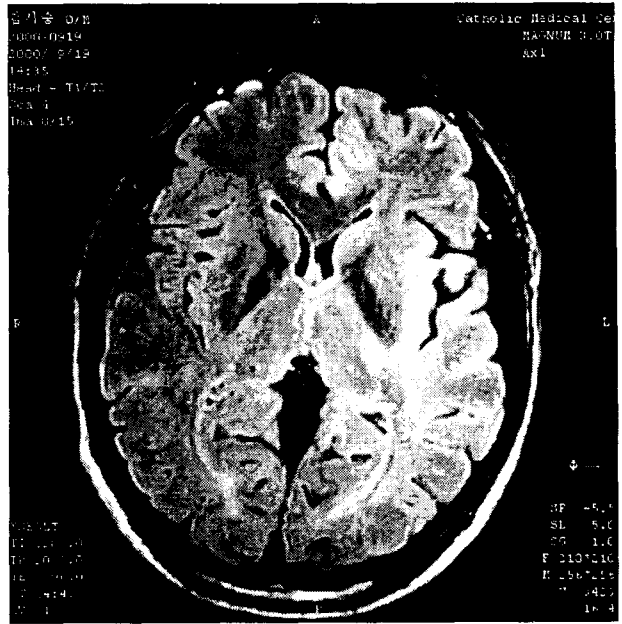


Figure 7. STIR image for fat suppression with TI 2200 ms, TR 9000 ms, TE 96 ms, NEX 1

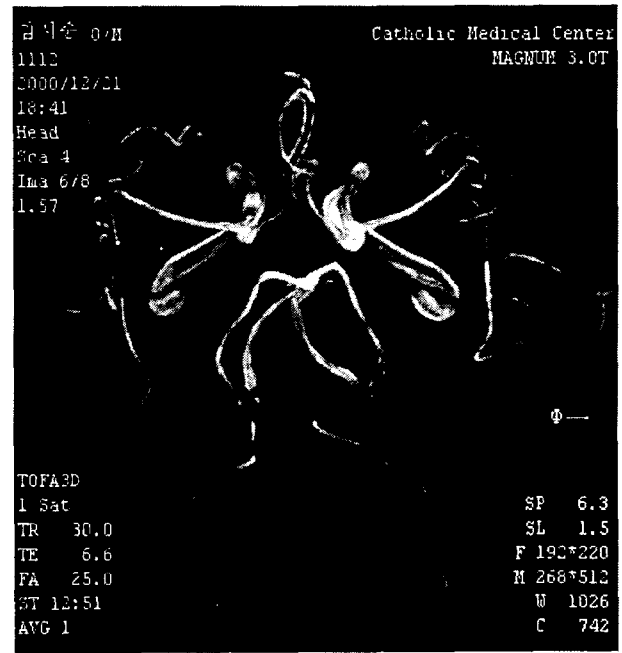
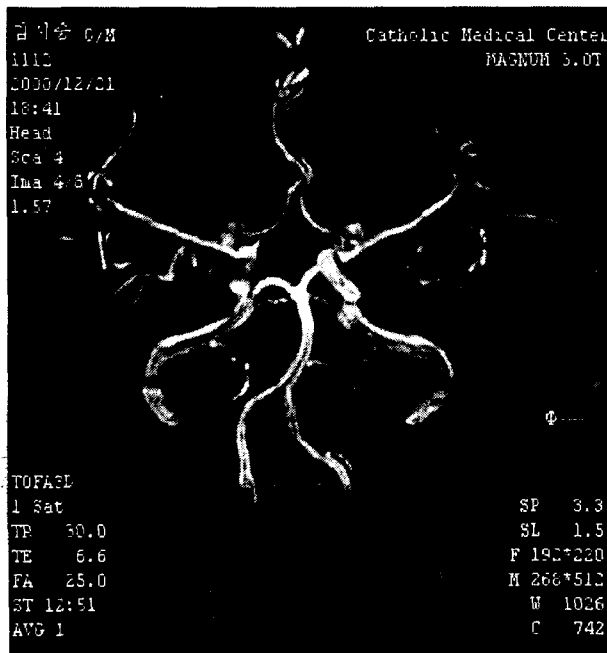


Figure 8. MR angiography is presented by 3D-time of flight (TOF) technique with TR 30 ms, TE 6.6 ms, FA 25°, NEX 1. Peripheral vessels are clearly demonstrated.

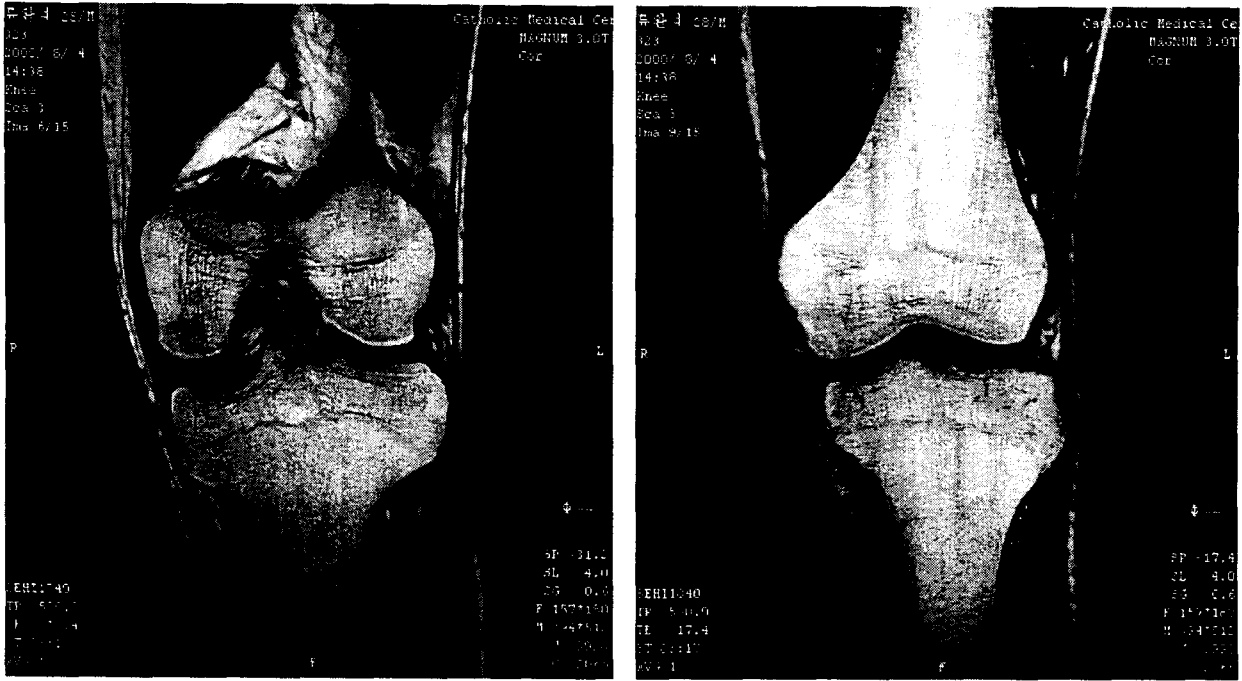


Figure 9. T1-weighted coronal MR images of knee. Conventional spin echo pulse sequence was used. We used TR 500 ms, TE 17.4 ms, NEX 1, slice thickness 4 mm and rectangular FOV 160x180 cm.

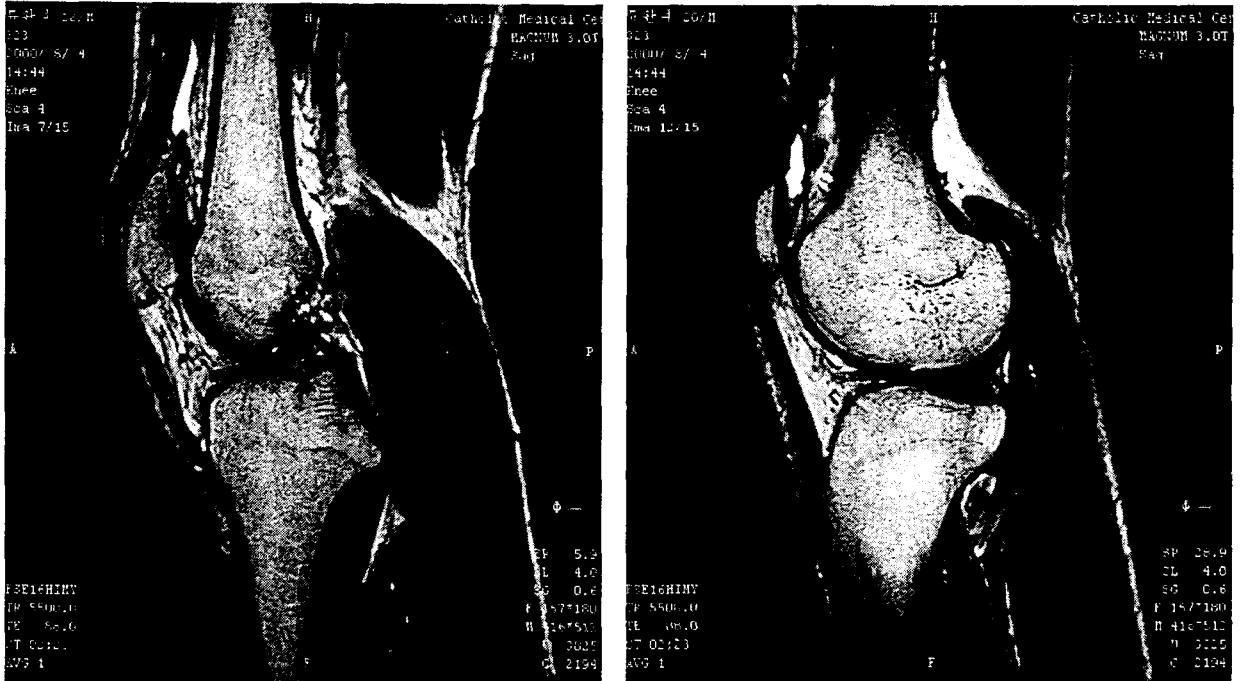


Figure 10. T2-weighted sagittal MR images of knee with FSE with ETL 16.

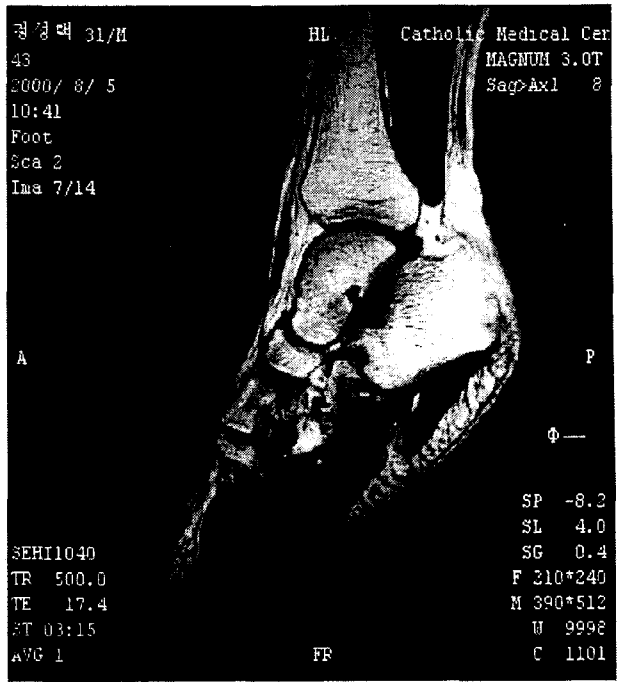
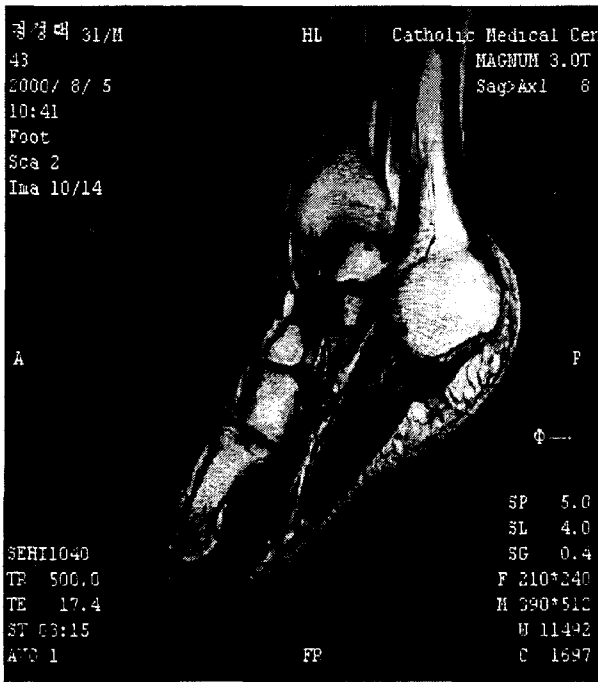


Figure 11. T1-weighted sagittal MR images of foot. Parameters are identical with the scans for knee.

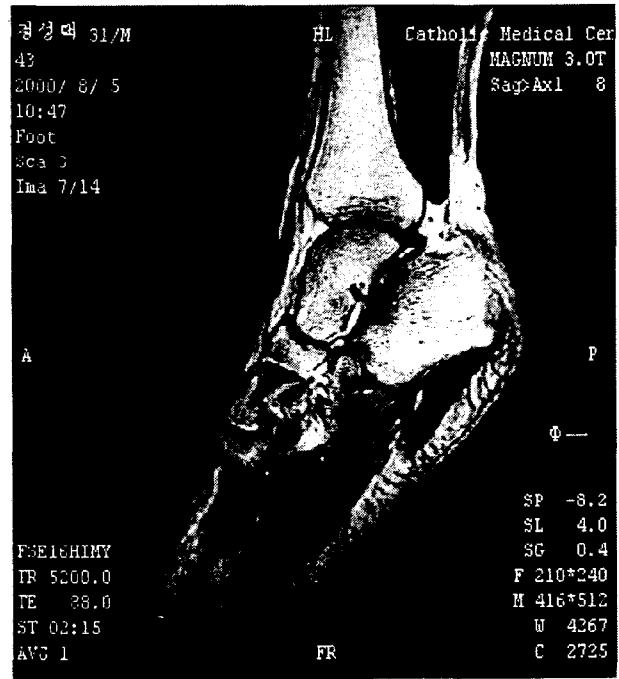


Figure 12. T2-weighted MR image of foot.

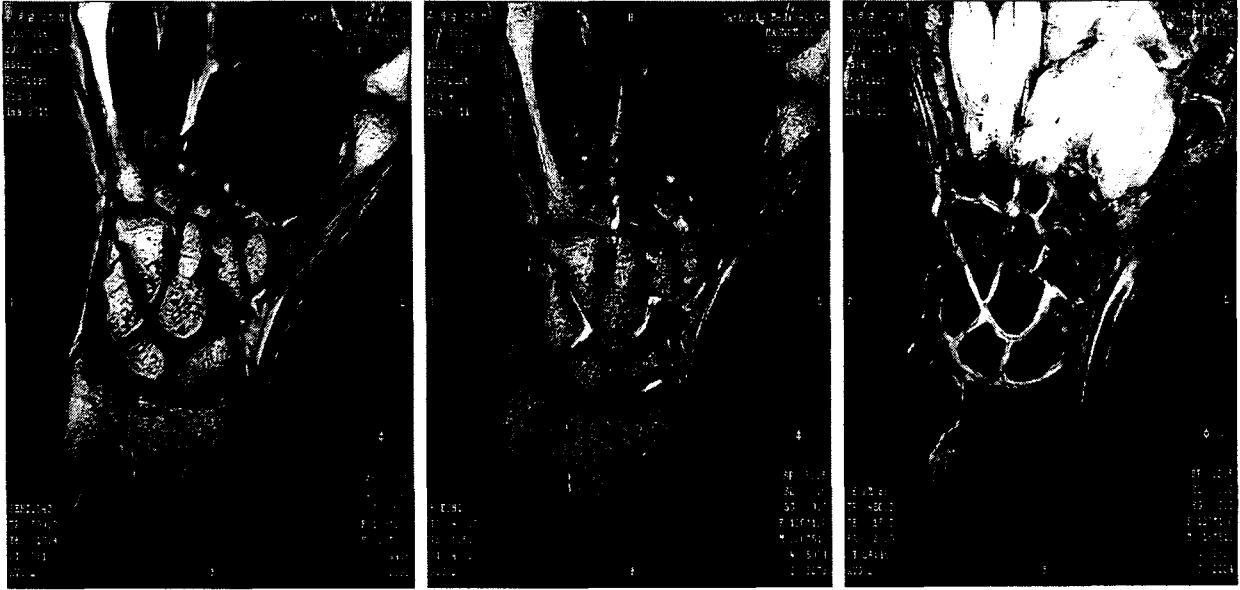


Figure 13. T1, T2 and T2-weighted MR images of wrist. In particular, we used gradient echo of spoil pulse in steady state (GESPHSSF) with TR 450 ms, TE 15 ms, NEX 2 and flip angle 22°. Total 10 segmental bone structures are well denoted.*